High-temperature KCl-induced corrosion of high Cr and Ni alloys investigated by in-situ diffraction

Phillip Kingsbery[1,2] ⓘ | **Anna M. Manzoni**[2] ⓘ | **P. Suarez Ocaño**[2] |
D. M. Többens[3] | **C. Stephan-Scherb**[4] ⓘ

[1]Department of Earth Science, Freie Universität Berlin, Berlin, Germany

[2]Materialography, Fractography and Ageing of Engineered Materials, Bundesanstalt für Materialforschung und -prüfung, Berlin, Germany

[3]Department Structure and Dynamics of Energy Materials, Helmholtz-Zentrum Berlin für Materialien und Energie, Berlin, Germany

[4]Institute of Geosciences and Geography, Martin-Luther-Universität Halle-Wittenberg, Halle (Saale), Germany

Correspondence
Phillip Kingsbery, Freie Universität Berlin, Malteserstraße 74-100, 12247 Berlin, Germany.
Email: phillip.kingsbery@fu-berlin.de

Funding information
Deutsche Forschungsgemeinschaft (DFG, German Research Foundation), Grant/Award Number: 416318834; HZB, Grant/Award Numbers: 192-08532-ST, 202-09765-ST

Abstract

High-temperature KCl-induced corrosion in laboratory air was observed in situ utilizing X-ray diffraction. High Cr-containing model alloys (Fe-13Cr, Fe-18Cr-12Ni, and Fe-25Cr-20Ni) were coated with KCl and exposed to dry air at 560°C. KCl-free alloys were studied in the equivalent atmosphere as a reference. After exposure to KCl-free environments, all alloys showed the formation of very thin oxide layers, indicating good corrosion resistance. In contrast, KCl-bearing alloys showed distinct damage after exposure.

K E Y W O R D S
deposit-induced corrosion, high-temperature corrosion, in-situ X-ray diffraction

1 | INTRODUCTION

With increasing efforts to combat climate change the issue of environmentally friendly power sources gains importance. As an intermediate step, the co-firing of coal power plants with biofuel has been used to lower the environmental impact of power generation by thermal power plants.[1] This has the benefit of using existing facilities while new technologies are being developed. The chemistry of biofuel and the resulting flue gas composition are different from the conditions present in purely coal/lignite-fired power plants. Straw, for example, contains significant amounts of KCl, which is known to cause severe corrosion, while coal contains only negligible amounts of KCl.[2,3]

The corrosion behavior is dependent on both the alloy itself and the environment. The amount of Cr alloyed in steel directly affects the corrosion products, which in turn affects the long-term stability of steel.[4,5]

High Cr-alloyed steels can form a protective Cr_2O_3 layer at high temperatures. However, in the presence of KCl, Cr-rich steels were shown to form K_2CrO_4 for the steels Sanicro 28 (550°C [20% O_2, 10% H_2O vol%][6]), 304L (600°C [5% O_2, 40% H_2O vol%][7]), and Fe-18Cr-10Ni (600°C [5% O_2, 40% H_2O vol%][8]). This reaction destroys the protective Cr_2O_3 scale causing further corrosion.

A deeper understanding of the corrosion mechanism is needed to design alloys that can withstand the corrosion attack for extended amounts of time. An important aspect of this is the onset of corrosion, i.e. which phases initially

form and which develop later. This is crucial to understanding the potentially beneficial properties of different elements in the atmosphere as shown by Karlsson et al., who demonstrated the benefits of SO_2 by converting KCl and K_2CrO_4 into K_2SO_4, protecting underlying Cr_2O_3 from further KCl attack. These reactions can happen rapidly, sometimes taking less than 30 min to fully convert (i.e., $4K_2CrO_4 + 4SO_2 \rightarrow 4K_2SO_4 + 2Cr_2O_3 + O_2$).[9]

The aforementioned shows the importance of understanding the underlying corrosion mechanism, demonstrating how alloying components and atmospheres affect the reaction rates and revealing potential engineering steps to optimize the corrosion rate.

Therefore, the goal of this study is to gain insight into the initial stages of corrosion by following the reactions in-situ during the first 5 h of exposure using synchrotron radiation. The effect of KCl is investigated as well as the impact of alloying elements Cr and Ni.

2 | MATERIALS AND METHODS

2.1 | Materials

The used alloys were vacuum melted, hot and cold rolled with minimum elemental purities of 99.95% for Fe and 99.9% for Cr and Ni, provided by Hauner GmbH. The chemical composition is listed in Table 1, further information can be found in a previous paper.[10]

These alloys were chosen as close representatives of commercially used alloys, such as X20, TP347H, and HR3C.[11]

2.2 | Sample preparation and exposure

The samples were cut into 20 mm × 10 mm × 3 mm sized coupons, then ground with SiC paper to grit size P1200.

Samples with KCl were sprayed with a KCl/H_2O solution while being heated to >100°C to achieve a thin ($<50\,\mu m$) KCl coating (an example of the sprayed,

TABLE 1 Elemental composition of model alloys obtained by electron microprobe analysis (EMPA) on a JEOL JXA 8200 Superprobe utilizing ZAF correction and salt load of coated samples.

Sample	Fe	Cr	Ni	Salt load
Fe-13Cr	Bal.	13.5 ± 0.4	0.0 ± 0.0	1.80 ± 1.00
Fe-18Cr-12Ni	Bal.	18.5 ± 0.5	11.8 ± 0.2	0.77 ± 0.04
Fe-25Cr-20Ni	Bal.	24.5 ± 0.7	19.1 ± 0.4	2.68 ± 0.04

Note: Values are given in wt% and $\frac{mg}{cm}^2$, respectively.

pre-exposed sample is shown in Figure 1, the salt load in Table 1). A thin coating was chosen to allow the observation of phases growing between the metal and KCl. All samples were weighed and their dimensions were measured before the experiment.

Diffraction experiments were conducted at the beamline KMC-2[12] of the synchrotron facility BESSY II, utilizing a 1 Å wavelength and a Bruker Vantec 2000 area scintillation detector. Measurements were done in grazing incidence geometry, with an incidence angle of 1° and a vertical beam size of 0.1 mm. Diffraction peaks from the graphite dome of the furnace were blocked by a detector aperture close to the dome. The sample was heated using an Anton-Paar DHS 1100 furnace, set to a temperature of 655°C with a heating rate of $200\frac{K}{min}$. A calibration run showed this setup to result in a surface metal temperature of ≈560°C. This temperature deviation is due to the gas flow setup used. During the experiment, samples were exposed to a stream of lab air $\left(100\,\frac{cm^3}{min}\right)$ inside the graphite dome. The setup is illustrated in Figure 2.
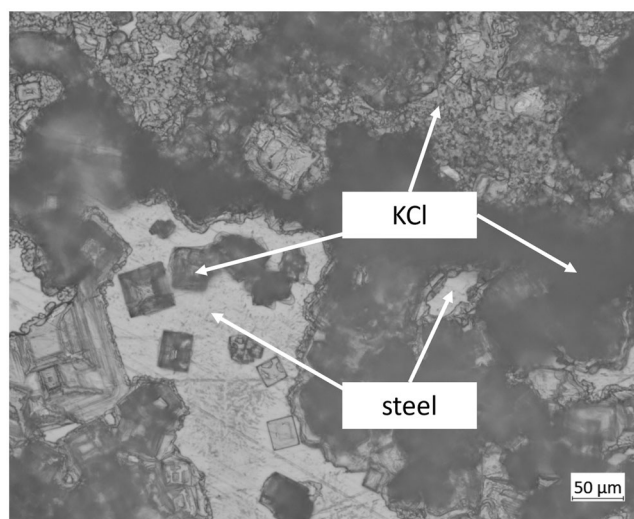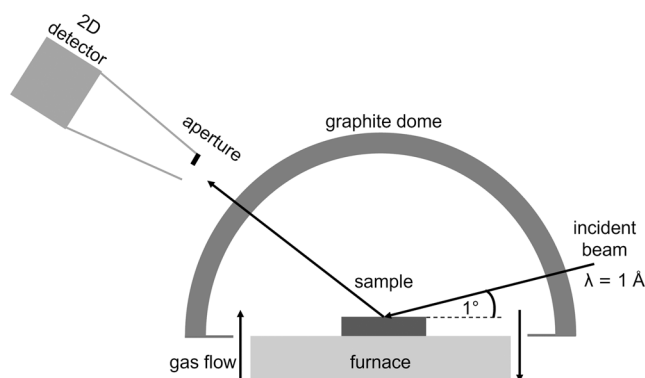
Samples were held for 5 h at this temperature, during which X-ray diffraction (XRD) data were collected back-to-back every 20 min. The incidence angle was held constant at 1°.

While experiments were conducted, the humidity of the atmosphere was measured before entering the graphite dome at ≈28°. The humidity is listed in Table 2, which translates to partial pressures of $0.04\,kPa < pH_2O < 0.13\,kPa$ (i.e., $<0.1\% H_2O$) using the Buck equation.[13,14]

FIGURE 1 Microscopy image of the sample surface coated with KCl before exposure.

FIGURE 2 Sketch of experimental setup. The incident beam passes through a graphite dome to graze the sample at a 1° angle. During the experiment, the sample is heated via a furnace, and gas flows through the dome. The diffracted beam is then recorded by a 2D detector.

TABLE 2 Relative humidity [%] of atmosphere during diffraction experiments.

Sample	Without KCl	With KCl
Fe-13Cr	3.49 ± 0.88	1.99 ± 0.19
Fe-18Cr-12Ni	1.52 ± 0.05	1.58 ± 0.09
Fe-25Cr-20Ni	1.40 ± 0.10	1.14 ± 0.07

Note: All values are given at $\approx 28°C$.

2.3 | Postexposure characterization

Immediately after the experiment, the samples were weighed three times on a Sartorius scale ($d = 0.01$ mg) to calculate an average. This weight was then used to calculate the weight difference to the pre-exposed, salt-coated (if applicable) sample and divided by the surface area of the pre-exposed sample to obtain the weight gain, which indicates how much atmospheric gas (i.e., oxygen) reacted with the steel to form a scale. A higher weight gain therefore implies a thicker scale. The surface was carbon-coated and analyzed by scanning electron microscopy (SEM) using a Zeiss Sigma 300 VP utilizing a 20 kV acceleration voltage.

Cross-sections were prepared by embedding the samples into an epoxy resin and final polishing with a $1 \mu m$ diamond solution for KCl-free samples. KCl bearing samples were dry polished down to P4000 grit with SiC paper to retain water-soluble phases. The cross-sections were then carbon-coated and analyzed by SEM.

Elemental distribution maps of the surfaces and cross-sections of samples were collected using Bruker Quantax Xflash 60 mm^2 silicon drift energy dispersive X-ray spectroscopy (EDS) detectors attached to the SEM.

3 | RESULTS AND DISCUSSION

3.1 | KCl-free samples

Figure 3a shows the surface backscatter electron (BSE) image of Fe-13Cr. The surface shows scratch marks caused by grinding of the sample pre-exposure and spherical corrosion products are preferentially situated along these scratches. The visibility of scratches indicates a thin scale.

The diffraction data displayed in Figure 4 shows no visible peaks until 100 min, where a broad 104 peak of $(Fe_xCr_{1-x})_2O_3$ appears at $2\Theta \approx 21.5°$. The other major peak of this phase, 110 (at $2\Theta \approx 23.0°$), is not visible, indicating an oriented growth. Over time the 104 peak gains intensity.

The cross-section BSE image of this sample is shown in Figure 5a. The cross-section confirms the surface observations. Only very small-scale particles ($<1 \mu m$) are found at the metal/gas interface and the overall corrosion attack is minimal.

The surface BSE image of Fe-18Cr-12Ni is shown in Figure 3b. The surface shows scratch marks and no corrosion product is visible.

The diffraction data shown in Figure 4 shows no visible oxide peaks. This indicates that, if ever an oxide scale is present, it is too thin to contribute significantly to diffraction.

The cross-section in Figure 5b shows a very thin corrosion layer ($<1 \mu m$) in accordance with the diffraction data.

Fe-25Cr-20Ni (Figure 3c) displays a similar surface to Fe-18Cr-12Ni. Scratch marks are visible and no corrosion product can be seen in the BSE image.

Figure 4 shows the XRD patterns of Fe-25Cr-20Ni collected during gas exposure. At $2\Theta = 21.5°$, a peak is observed after 100 min of exposure, which increases in intensity with exposure time. This corresponds to the 104 reflection of $(Fe_xCr_{1-x})_2O_3$.

The cross-sectional SEM image is shown in Figure 5c. As in Fe-13Cr and Fe-18Cr-12Ni, only a small amount of corrosion product is observed in the cross-section.

The weight gain of samples is displayed in Figure 6 and shows no remarkable increase for any studied alloy in the absence of KCl. This means that no significant corrosion is observed after 5 h of exposure to laboratory air at 560°C. The difference is negligible across alloying content. The low weight gain of samples corresponds to alloys Fe-13Cr, Fe-18Cr-12Ni, and Fe-25Cr-20Ni shown in the BSE images of Figure 3a–c, respectively. The surfaces of all samples show no covering of any oxide layer after 5 h exposure to laboratory air at 560°C. The grinding scratches are still visible and corrosion
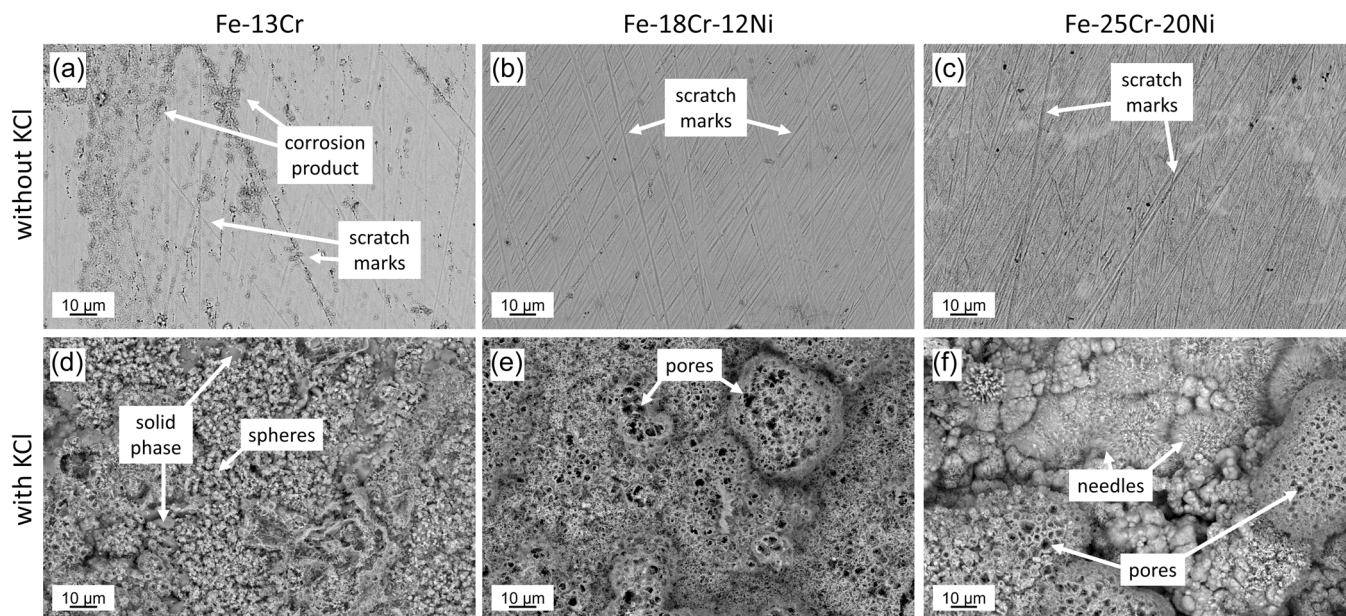
FIGURE 3 SEM BSE surface images of samples. The top row shows samples exposed to dry air (a–c), and the bottom, those exposed to dry air and coated with KCl (d–f). BSE, backscatter electron; SEM, scanning electron microscopy.
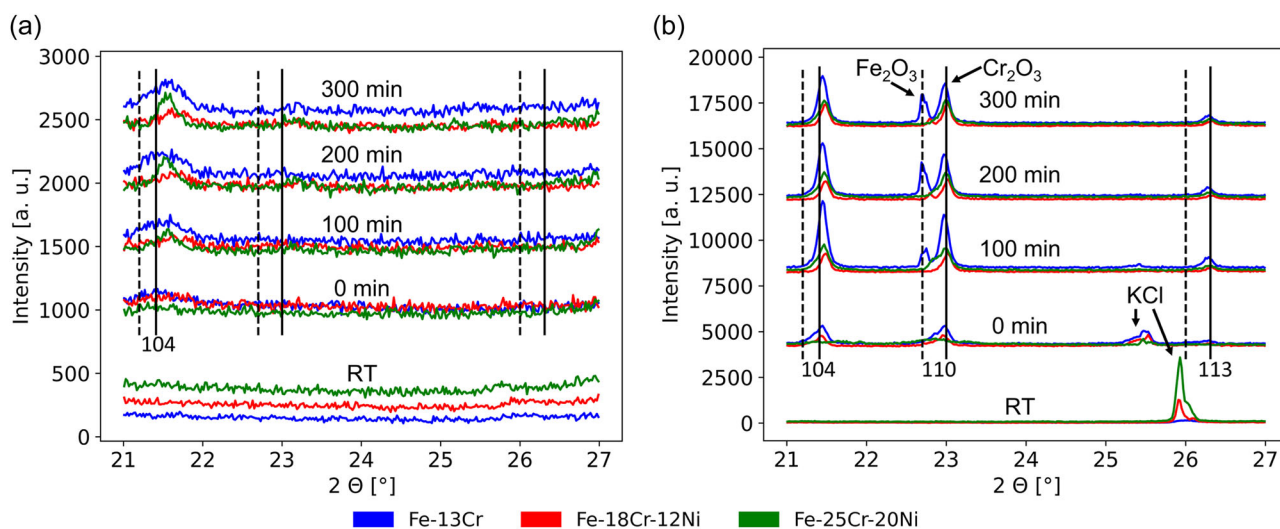
FIGURE 4 Diffraction pattern for different exposure times of samples. The graphs show the change in intensity over time. Figure (a) shows samples exposed to dry air, and Figure (b) to dry air with KCl coating. The lines from bottom to top show measurements later during the exposure. RT shows the initial room temperature measurement and the duration (in min) of the time passed since reaching the experimental surface temperature of 560°C. Theoretical peak positions of Cr_2O_3 (black lines) and Fe_2O_3 (dashed lines) at 560°C were calculated for guidance.[15–18] The Fe-25Cr-20Ni data in Figure A has been shifted by 0.2° to account for a potential height error, based on the peak position of the bulk material. [Color figure can be viewed at wileyonlinelibrary.com]

damage is negligible. Assuming the scale is compact and comprised of $Cr_2O_3\left(\rho = 5.22\frac{g}{cm^3}\right)$, the expected scale thickness based on the weight gain in Figure 6 is around 0. 1-0.3 μm.[19]

The high Cr content in the studied alloys supports the growth of a thin and protective oxide layer. The first signs of growth were observed after 100 min of exposure by the increase of the 104 reflection.
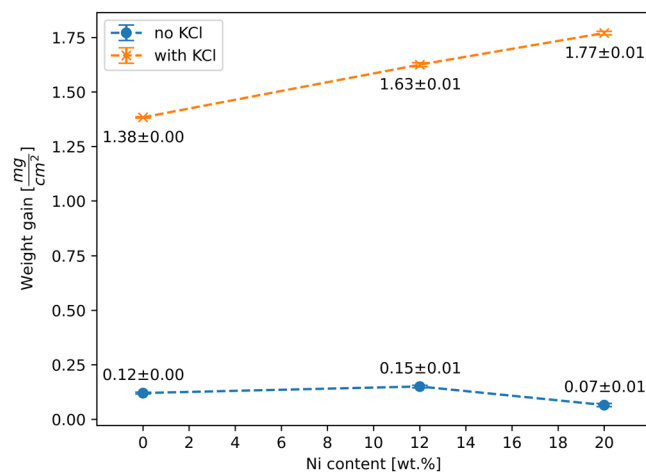
3.2 | Samples with KCl

Figure 3d–f shows the surface BSE images of samples coated with KCl exposed to dry air.

The surface of Fe-13Cr (Figure 3d) is covered in scale and shows two distinct phases indicated by arrows: a slightly darker solid phase and a lighter phase consisting of multiple small spheres. The spheres leave space for the
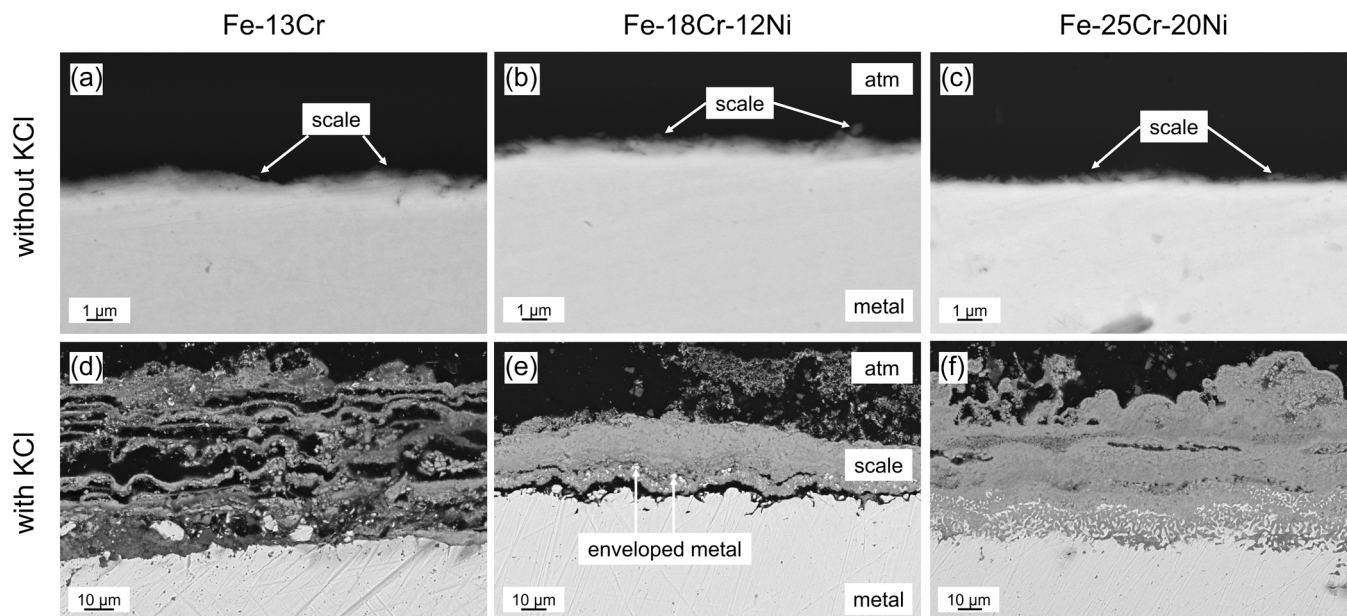
FIGURE 5 SEM BSE cross-section images of samples after 5 h exposure at 560°C surface temperature. The top row shows samples exposed to lab air (a–c), and the bottom, samples in lab air coated with KCl (d–f). BSE, backscatter electron; SEM, scanning electron microscopy.

FIGURE 6 Weight gain of Fe-13Cr, Fe-18Cr-12Ni, and Fe-25Cr-20Ni after 5 h exposure time normalized to their surface area. Specimens coated with KCl are marked with a cross and uncoated samples are indicated by a circle. Error bars are within the symbol. [Color figure can be viewed at wileyonlinelibrary.com]

gas to penetrate the scale, allowing for access to the metal surface.

The diffraction data depicted in Figure 4 shows Fe_2O_3 ($2\Theta = 22.7°$) and Cr_2O_3 ($2\Theta = 21.5°, 23.0°, 26.3°$) peaks. Cr_2O_3 is already formed before reaching experimental temperature (i.e., before 0 min), while the Fe_2O_3 110 reflection shows significant intensity from 100 min onwards. The 110 ($2\Theta = 22.7°$) peak gains in intensity over time but 104 ($2\Theta = 21.2°$) of Fe_2O_3 is not detected. Since in powder diffraction diagrams of Fe_2O_3 the 110 and 104 have similar intensities, the higher 110 and absence of the 104 peak indicate a highly oriented crystal growth of Fe_2O_3 in [110]. Most of the Cr_2O_3 phase growth occurs between RT and 100 min. Fe_2O_3 forms later, mainly between 0 and 200 min.

The cross-section (Figure 5d) shows a multilayered scale. The corrosion attack seems to happen uniformly— there are no signs of a faster attack along alloy grain boundaries. EDS analysis elemental mappings (Figure 8) show a Cl-bearing phase at the metal/scale interface and a significant K-bearing phase at the scale/gas interface. EDS shows Fe and O in the same spot as Cl, indicating both iron chlorides and iron oxides. K shares its distribution with Cr and O, indicating potassium chromate (K_2CrO_4).

Fe-18Cr-12Ni shows a very porous scale in Figure 3e. Multiple large pores can be seen, effectively reducing transport lengths through the scale.

The diffraction data (Figure 4) shows only a single Cr_2O_3 phase up to 100 min. Starting at 200 min, the 110 peak of Fe_2O_3 is observed at a slightly higher angle than in Fe-13Cr (22.8° vs. 22.7°). This might be due to a higher abundance of Cr in $(Fe_xCr_{1-x})_2O_3$. The peak intensity and peak growth throughout the experimental length are lower compared to Fe-13Cr. The KCl peak seen at room temperature disappears almost completely by the time the sample reaches 560°C (0 min in Figure 4b).

The cross-section seen in Figure 5e shows a much more compact scale compared to Fe-13Cr. At the metal/scale interface, remnants of the original metal can be seen enveloped by the forming scale.

The scale consists of a Cr-rich oxide toward the metal side and a Fe-rich oxide toward the gas side (see Figure 8). Based on the observations from Figure 4, these oxides are Cr_2O_3 and Fe_2O_3.

Fe-25Cr-20Ni shows a porous scale akin to Fe-18Cr-12Ni (Figure 3e,f) and small needle-like structures. The pores allow for shorter transport paths of the gas through the scale.

The diffraction data shown in Figure 4 displays the development of Cr_2O_3. The phase forms primarily between 0 and 100 min. Additionally, the 110 peak of Cr_2O_3 ($2\Theta = 23.0°$) has a shoulder toward lower diffraction angles, indicating a secondary reflection. This would fit the 110 orientation of the $(Fe_xCr_{1-x})_2O_3$ peak. Since Fe_2O_3 and Cr_2O_3 can form the solid solution $(Fe_xCr_{1-x})_2O_3$, the peak shoulder toward lower angles indicates a decreasing amount of Fe in $(Fe_xCr_{1-x})_2O_3$ over time.[20] The KCl peak disappears between the room temperature measurement and the first measurement at 560°C.

The cross-section (Figure 5f) shows multiple layers and extensive inner damage to the material. Below the original alloy surface, chromium oxide is observed deep in the base metal (Figure 8).

The scale of Fe-25Cr-20Ni consists of multiple layers alternating between Cr_2O_3 and Fe_2O_3 layers. Based on the repetitive pattern within these layers, it is likely that a Cr_2O_3 + Fe_2O_3 layer forms, which then separates from the underlying metal, causing a new layer to form. The buckling might be caused by the internal oxidation of Cr, causing a volume increase, which induces stress.[21,22]

The metal also shows Cr depletion underneath the closest Cr_2O_3 layer, indicating a high Cr consumption by chlorination and oxidation, or a slow Cr diffusion within the metal. Tökei et al. have shown that the diffusion rates of Cr between steels with the same microstructure but different elemental compositions are fairly similar (i.e., D_V (γ-20Cr32Ni) $= 6.06 \times 10^{-20}$ $\frac{m^2}{s}$ vs. $D_V(\gamma$-18Cr8Ni) $= 1.04 \times 10^{-19}$ $\frac{m^2}{s}$ at 881K).[23] Since both alloys (Fe-18Cr-12Ni and Fe25Cr-20Ni) exhibit a ferritic-austenitic microstructure, the overall diffusion behavior of chromium in the alloy should be comparable.[10] Because Fe-18Cr-12Ni does not show such an extensive Cr depletion (see Figure 7), a higher Cr consumption of the bulk alloy to form Cr chlorides and oxides is the probable cause. Potassium chromate (K_2CrO_4) is observed toward the scale gas interface, see Figure 8.

Samples coated with KCl show significantly more corrosion than their uncoated counterparts. When comparing the SEM BSE cross-section images shown in Figure 5 it is evident that the samples with KCl form a
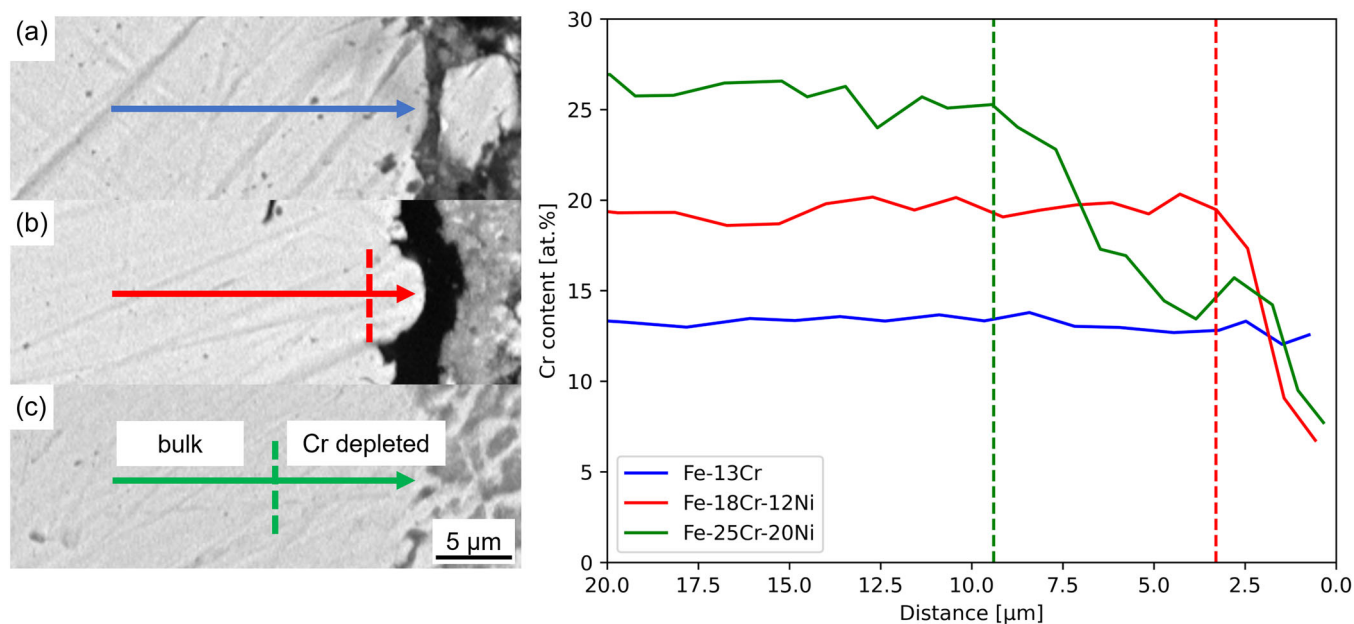

FIGURE 7 Cr content near the surface of salt-bearing samples. The *x*-axis denotes the distance from the surface for samples Fe-13Cr and Fe-18Cr-12Ni. Due to the internal corrosion of Fe-25Cr-20Ni, the distance for this sample represents the distance to the closest internal corrosion layer. The dashed lines indicate the border between the bulk alloy and the Cr-depleted region. The BSE images show the measurement positions in Fe-13Cr (a), Fe-18Cr-12Ni (b), and Fe-25Cr-20Ni (c). BSE, backscatter electron. [Color figure can be viewed at wileyonlinelibrary.com]
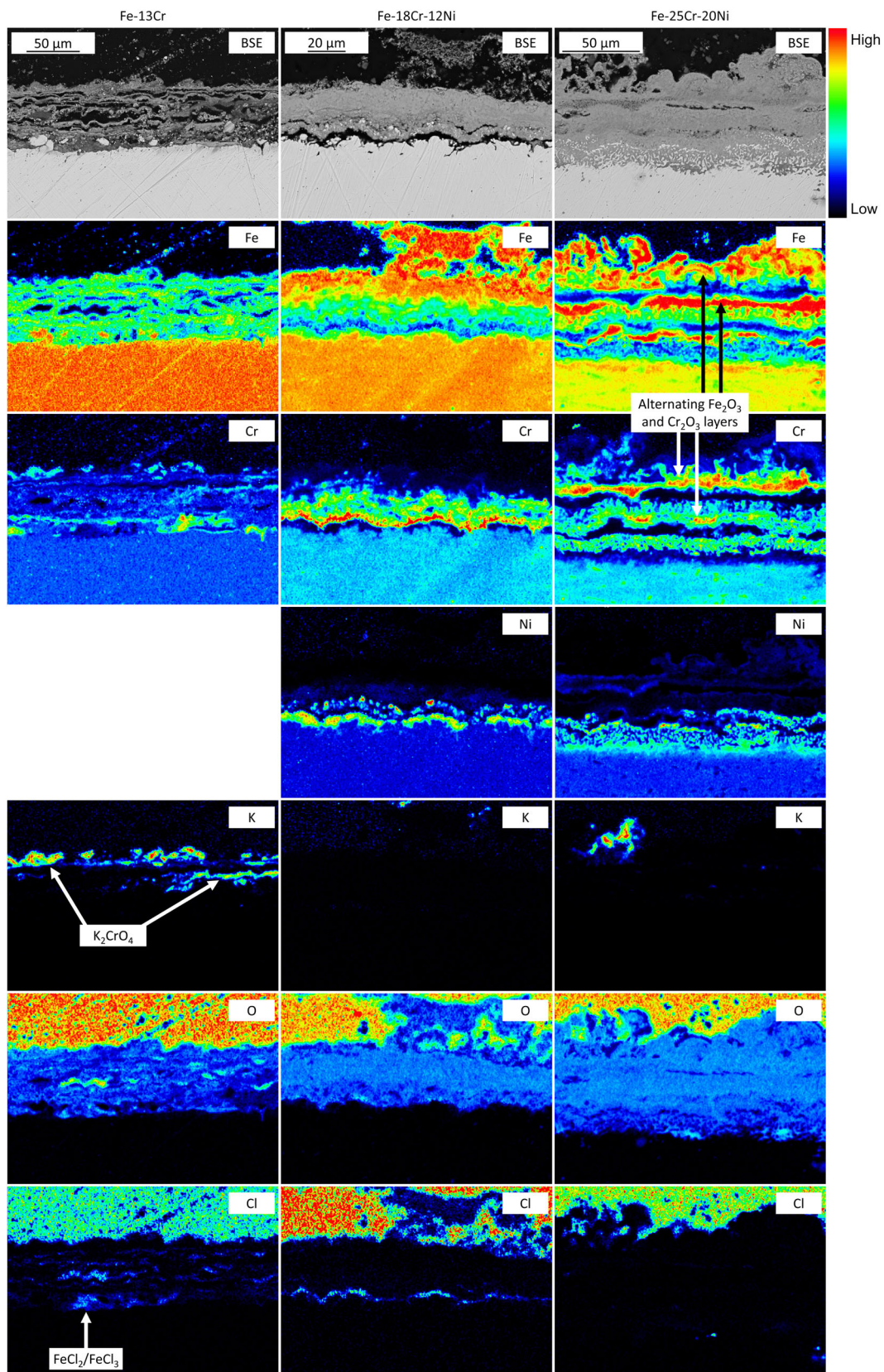
FIGURE 8 EDS elemental mappings of samples Fe-13Cr, Fe-18Cr-12Ni, and Fe-25Cr-20Ni (from left to right) coated with KCl after 5 h exposure to dry air. EDS, energy dispersive X-ray spectroscopy. [Color figure can be viewed at wileyonlinelibrary.com]

large layer of corrosion product while samples without KCl show barely any.

The weight gain (displayed in Figure 6) supports this, showing that samples coated with KCl exhibit a much higher mass gain than non-coated samples. Adding KCl to the sample causes the weight gain to increase by about one order of magnitude, demonstrating a much poorer corrosion resistance. Furthermore, increasing the amount of Cr and Ni in the alloy causes a higher weight gain in the presence of KCl. Thus, increasing the amount of Cr and Ni in the alloy does not increase corrosion resistance in the presence of KCl.

In literature, the performance of steels has been shown to depend on alloying content, temperature, microstructure, and environment, making direct comparisons between model alloys and commercial steels difficult due to commercial steels containing microalloying elements and differing microstructures.[24,25] Natesan et al. showed that at high temperatures (800°C), 347HFG (18Cr-11Ni steel) shows lower scaling and penetration rate compared to HCM12A (12Cr steel) under ash + sulfates + NaCl deposits. However, at lower temperatures (650°C), the opposite was observed. The higher alloyed HR3C (25Cr-20Ni steel) shows lower scaling and penetration rates than both of the aforementioned steels at 650°C and 800°C.[24] Furthermore, Natesan et al. showed that the performance of steels is not solely linked to the Cr and Ni content at 650°C, with some high Ni steels (like NF709, a 20Cr-25Ni steel) showing higher scaling and penetration rates than HCM12A, while others showed very comparable (800H, a 21Cr-32Ni steel) or lower rates, which were more comparable to HR3C (like HR120, a 25Cr-37Ni steel).

Previous studies on the effect of KCl on steels in SO_2-bearing atmospheres show the role of active Cl corrosion.[10,26–28] This process involves the creation of Fe and Cr chlorides, which initially form as a solid due to the Cl attack of the metal. These chlorides can then evaporate and rise toward the surface. Once they have reached it, the oxygen partial pressure is high enough to oxidize the metal chlorides creating new Cl_2, which can attack the metal again. A similar process is presumed to happen here. The KCl disappears rapidly (Figure 4), indicating a fast reaction of KCl, leaving Cl to react with the steel-forming metal chlorides (see Fe-13Cr in Figure 8 Cl). During this time, Cr_2O_3 and Fe_2O_3 form (Figure 4) in much larger quantities than in the uncoated samples. This indicates the catalytic effect of Cl_2, continuously forming metal chlorides, which then turn into metal oxides and chlorine, allowing renewed chlorination of the metal.
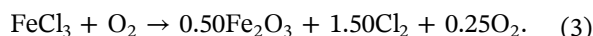
The absence of KCl in the diffraction diagram (Figure 4b) and K in the EDS measurement (Figure 8) indicates that a K-bearing gas is formed under these conditions alongside Cl_2. The Cl_2 would then attack the metal forming Fe and Cr chlorides, which can partially form gases due to their high vapor pressure.[29] The following presumed reactions were calculated using FactSage.[30] The initial reaction is shown using Fe-13Cr as an example (gas phases seen in Table 3).
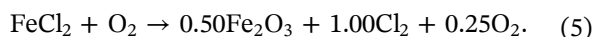
$$Fe_{0.86}Cr_{0.14} + 1.5Cl_2 \rightarrow gas + 0.14CrCl_3 \\ + 1.1*10^{-2}FeCl_2. \tag{1}$$
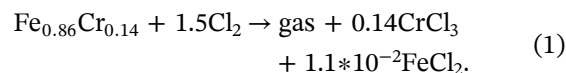
$$\Delta G = -5.9*10^5 J. \tag{2}$$

The gaseous metal chlorides then react with oxygen to form metal oxides and new Cl_2 (cutoff $<10^{-1}$ moles).

$$FeCl_3 + O_2 \rightarrow 0.50Fe_2O_3 + 1.50Cl_2 + 0.25O_2. \tag{3}$$

$$\Delta G = -8.2*10^5 J. \tag{4}$$

$$FeCl_2 + O_2 \rightarrow 0.50Fe_2O_3 + 1.00Cl_2 + 0.25O_2. \tag{5}$$

$$\Delta G = -7.2*10^5 J. \tag{6}$$

$$CrCl_4 + O_2 \rightarrow 0.48Cr_2O_3 + 1.93Cl_2 + 0.26O_2. \tag{7}$$
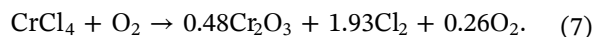
$$\Delta G = -1.1*10^6 J. \tag{8}$$

The Cl_2 formed in the reactions shown above can initiate the reaction (1), resulting in a continuous corrosion attack.

Samples in contact with KCl show buckling of corrosion layers in these experiments. This might be due to buckling of the scale, leading to the formation of multiple scale layers (Figure 5). Michalik et al. showed that in the Ar-O_2 atmosphere void formation is observed, leading to buckling of the scale.[31] These observations can also be made for the investigated samples sprayed with KCl (Figure 5), which show a multilayered scale. Every time a new layer is formed, additional metal and oxygen are consumed, inducing weight gain.

Additionally, coated samples show a porous surface (Figure 3), which might be due to a gaseous phase forming through volatilization or oxidation of Cr_2O_3 to CrO_3.[32]

TABLE 3 Gas phases in reaction (1), cutoff $<10^{-4}$ mol.

Gas phase	Amount [mol]
$(FeCl_3)_2$	0.40
$FeCl_3$	0.06
Cl_2	$5.3*10^{-3}$
$CrCl_4$	$2.8*10^{-4}$
$FeCl_2$	$1.3*10^{-4}$

Pores could also form due to the formation of gaseous metal chlorides at the metal scale interface. As discussed before, corrosion due to chlorides causes the formation of volatile metal chlorides. These chlorides could lead to pores, which allow for faster transport of Cl_2 to the metal and therefore accelerate corrosion rates. The porous surface could lead to better access of the atmospheric oxygen and chlorine to the alloy surface through shorter diffusion paths, increasing the reaction rate. Cr depletion is observed in both Ni-bearing samples visible in Figures 7 and 8.

Figure 7 shows the Cr content relative to the distance of the nearest Cr sink (surface/internal corrosion). Fe-13Cr does not show a significant Cr depletion toward the surface. By comparison, both higher alloyed samples (Fe-18Cr-12Ni and Fe-25Cr-20Ni) show severe Cr depletion. Fe-18Cr-12Ni deviates from its average Cr content at around $3\,\mu m$, with a maximum Cr loss of $\approx 13\,at\%$. Fe-25Cr-20Ni shows Cr depletion around $9\,\mu m$, losing a maximum of $\approx 17\,at\%$.

The Cr depletion in Fe-18Cr-12Ni and Fe-25Cr-20Ni indicates a large Cr consumption, which might lead to poorer long-term performance due to reduced Cr availability for Cr_2O_3 formation. The larger depletion of Cr in Fe-25Cr-20Ni is probably caused by the formation of multiple buckling Cr_2O_3/Fe_2O_3 layers (as seen in Figure 8), repeatedly consuming Cr in the process. Fe-18Cr-12Ni only forms a single Cr_2O_3 layer by comparison, which seems to protect the underlying metal better from oxygen attack, reducing Cr consumption.

The larger Cr depletion and weight gain of Ni-bearing samples compared to Fe-13Cr indicates a negative effect of Ni on the corrosion behavior of the tested steels (see Figures 6 and 7). Cross-sections of samples show an internal attack of Ni alloyed steels (Figure 5e,f) that increases with alloying content, presumably due to the Ni itself or the change of the crystal lattice from body-centered cubic (bcc) to face-centered cubic (fcc), which lowers the diffusion rate within the metal.[33–35] The slower diffusion rate could be contributing to the Cr depletion seen in the Ni alloyed steels of the present study (Figure 7), especially if buckling of the scale occurs, as seen in Figure 5f.

4 | CONCLUSION

The impact of KCl on the first 5 h of steel corrosion in air was investigated in situ using synchrotron radiation.

Samples exposed to air show minimal corrosion and an oriented growth, while samples coated with KCl develop a much larger scale consisting primarily of $(Fe_xCr_{1-x})_2O_3$.

The addition of KCl leads to higher weight gain of all model alloys, with increasing severity for higher alloyed samples. The larger scale of KCl-coated samples is linked to multiple factors:

- Iron oxides: The addition of KCl causes the formation of Fe_2O_3 or $(Fe_xCr_{1-x})_2O_3$ after the initial formation of Cr_2O_3, which is less protective than Cr_2O_3.
- Cr depletion: Higher alloyed samples showed Cr depletion, which prevents the formation of new Cr_2O_3 layers after spallation events.
- Cl gas phases: Cl_2 causes the formation of volatile metal chloride phases, which leads to active corrosion.

Avoiding KCl is therefore of utmost importance to preserve the long-term stability of boiler tubes in power plants. Additionally, higher alloyed steels performed worse than Fe-13Cr, presumably due to Cr depletion and internal oxidation. Ni-alloyed steels therefore are not beneficial in this type of environment.

The results seen in these in-situ measurements reveal that faster measurements are necessary to observe the time-resolved growth of Cr_2O_3 and the disappearance of KCl. In particular, the heating time of the sample should be shortened via higher heating rates and the acquisition time reduced by narrowing the 2Θ range.

AUTHOR CONTRIBUTIONS
Phillip Kingsbery: Conceptualization; investigation; analysis; writing—original draft; visualization. **Anna M. Manzoni**: Analysis; writing—review and editing; experimental assistance. **C. Stephan-Scherb**: Conceptualization; analysis; writing—review and editing. **P. Suarez-Ocaño** and **D. M. Többens**: Experimental assistance. Open Access funding enabled and organized by Projekt DEAL.

CONFLICT OF INTEREST STATEMENT
The authors declare no conflict of interest.

DATA AVAILABILITY STATEMENT
The raw data required to reproduce these findings cannot be shared at this time as the data also forms part of an ongoing study.

ORCID
Phillip Kingsbery http://orcid.org/0000-0002-0401-2450
Anna M. Manzoni http://orcid.org/0000-0001-7252-9286
C. Stephan-Scherb https://orcid.org/0000-0001-6775-0023

REFERENCES

[1] D. Nicholls, J. Zerbe, General Technical Report PNW-GTR-867, United States Department of Agriculture **2012**, 1.

[2] Y. Shao, J. Wand, F. Preto, J. Zhu, C. Xu, *Energies* **2012**, *5*, 5171.

[3] H. P. Nielsen, F. J. Frandsen, K. Dam-Johansen, L. L. Baxter, *Prog. Energy Combust. Sci.* **2000**, *26*, 283.

[4] *Corrosion: Fundamentals, Testing, and Protection* (Eds. S. D. Cramer, B. S. Covino, Jr.), Vol. 13A, ASM Handbook, Materials Park **2003**.

[5] N. Othman, N. Othman, J. Zhang, D. Young, *Corros. Sci.* **2009**, *51*, 3039.

[6] J. Lehmusto, M. Sattari, M. Halvarsson, L. Hupa, *Corros. Sci.* **2021**, *183*, 109332.

[7] T. Jonsson, J. Froitzheim, J. Pettersson, J. -E. Svensson, L. -G. Johansson, M. Halvarsson, *Oxid. Met.* **2009**, *72*, 213.

[8] J. Pettersson, H. Asteman, J.-E. Svensson, L.-G. Johansson, *Oxid. Met.* **2005**, *64*, 23.

[9] S. Karlsson, T. Jonsson, J. Hall, J. Svensson, J. Liske, *Energy Fuels* **2014**, *28*, 3102.

[10] P. Kingsbery, C. Stephan-Scherb, *Mater. Corros.* **2022**, *73*, 758.

[11] K. Yoo, Y. He, S. Bae, D. Kim, *KEPCO J. Electr. Power Energy* **2018**, *4*, 25.

[12] Helmholtz-Zentrum Berlin für Materialien und Energie, *JLSRF* **2016**, *2*, A49.

[13] A. Buck, *J. Appl. Meteorol. Climatol.* **1981**, *20*, 1527.

[14] Buck Research Instruments, Model Cr-1A Hygrometer With Autofill, Operating Manual, Boulder **2012**.

[15] R. L. Blake, R. E. Hessevick, T. Zoltai, L. W. Finger, *Am. Mineral.* **1966**, *51*, 123.

[16] L. W. Finger, R. M. Hazen, *J. Appl. Phys.* **1980**, *51*, 5362.

[17] Y. Fei, *Thermal Expansion*, American Geophysical Union, Washington **1995**.

[18] Y. S. Touloukian, R. K. Kirby, E. R. M. Taylor, T. Y. R. Lee, Thermophysical Properties of Matter—the TPRC Data Series. Vol. 13. Thermal Expansion—Nonmetallic Solids **1977**.

[19] M. O'Neil, *The Merck Index—An Encyclopedia of Chemicals, Drugs, and Biologicals*, Royal Society of Chemistry, London **2013**.

[20] T. Grygar, P. Bezdicka, J. Dedecek, E. Petrovsky, O. Schneeweiss, *Ceram. Silik.* **2003**, *47*, 32.

[21] E. E. Newnham, Y. M. De Haan, *Z. Kristallogr. Cryst. Mater.* **1962**, *117*, 235.

[22] M. E. Straumanis, C. C. Weng, *Am. Mineral.* **1956**, *41*, 437.

[23] Z. Tőkei, K. Hennesen, H. Viefhaus, H. Grabke, *Mater. Sci. Technol.* **2000**, *16*, 1129.

[24] K. Natesan, J. Park, *Int. J. Hydrogen Energy* **2007**, *32*, 3689.

[25] F. Falk, O. Sobol, C. Stephan-Scherb, *Corros. Sci.* **2021**, *190*, 109618.

[26] H. Grabke, E. Reese, M. Spiegel, *Corros. Sci.* **1995**, *37*, 1023.

[27] Y.Y. Lee, M.J. McNallan, *Metall. Trans. A* **1987**, *18*, 1099.

[28] A. Z. M. Spiegel, H. Grabke, *Mater. High Temp.* **2003**, *20*, 153.

[29] A. Zahs, M. Spiegel, H. J. Grabke, *Corros. Sci.* **2000**, *42*, 1093.

[30] C. Bale, E. Bélisle, P. Chartrand, S. Decterov, G. Eriksson, A. Gheribi, K. Hack, I. Jung, Y. Kang, J. Melançon, A. Pelton, S. Petersen, C. Robelin, J. Sangster, P. Spencer, M. Van Ende, *Calphad* **2016**, *54*, 35.

[31] M. Michalik, M. Hänsel, J. Zurek, L. Singheiser, W. Quadakkers, *Mater. High Temp.* **2005**, *22*, 213.

[32] B. B. Ebbinghaus, *Comb. Flame* **1993**, *93*, 119.

[33] A. W. Bowen, G. M. Leak, *Metall. Trans. A* **1970**, *603*, 1695.

[34] F. S. Buffington, K. Hirano, M. Cohen, *ACTA Metall.* **1961**, *9*, 434.

[35] K. Hirano, M. Cohen, B. L. Averbach, *ACTA Metall.* **1961**, *9*, 440.